CrossMark

JFM RAPIDS
journals.cambridge.org/rapids

On the mechanisms that sustain the inception of attached cavitation

Omri Ram[1], Karuna Agarwal[1] and Joseph Katz[1],†

[1]Department of Mechanical Engineering, Johns Hopkins University, Baltimore, MD 21218, USA

This experimental study addresses the longstanding question of why inception of attached cavitation on curved surfaces or hydrofoils at incidence is relatively insensitive to the concentration of free-stream nuclei. High-speed imaging and high-resolution particle image velocimetry measurements examine cavitation inception on three curved surfaces with varying pressure minima followed by regions with adverse pressure gradients. When these pressure gradients either thicken the boundary layer or cause local flow separation, thin (50–60 μm) low-momentum zones form close to the wall. Microbubbles trapped in these regions are generated initially from the collapse of intermittent attachment of travelling bubble cavitation. These bubbles migrate slowly upstream for a few milliseconds either under the influence of the adverse pressure gradients when the flow remains attached or carried by the recirculating flow when the boundary layer is separated. Their speed is only 2 %–4 % of the free-stream velocity, and their trajectories are erratic, indicating near-dynamic equilibrium. Owing to the low local pressure, their diameter increases by two to four times by non-condensable gas diffusion, from 10 to 30 μm to the thickness of the low-momentum zone. At that time, either they are swept downstream by the free-stream flow or they become nuclei for new attached cavitation events. When the new patches collapse, new microbubbles form and the process repeats itself frequently, and independently of the free-stream nuclei. These phenomena do not occur when the adverse pressure gradients are too mild to create low-momentum zones with sufficient thickness to facilitate the slow upstream migration and growth.

Key words: cavitation

1. Introduction

Cavitation inception typically occurs when the local pressure in a liquid drops below the vapour pressure, causing explosive growth and collapse of bubbles in microsecond time scales. This condition is characterized using the cavitation index,

† Email address for correspondence: katz@jhu.edu

$\sigma = (P_{in} - P_v)/0.5\rho V_{in}^2$, where P_{in}, P_v, ρ and V_{in} are reference pressure, vapour pressure, water density and a reference speed, respectively (e.g. Arndt 2002; Brennen 2013). Previous laboratory studies involving cavitation attached to surfaces have shown that, just below the inception pressure, the cavitation appears as a thin glossy sheet with either a sharp- or blunt-shaped leading edge, depending on the surface roughness (Arakeri & Acosta 1973; Gates & Acosta 1979; Katz 1984; Gopalan & Katz 2000). Parkin & Kermeen (1953) were the first to report the application of high-speed imaging to observe the inception process on a hemispherical headform. They showed that stationary thin cavitation patches form past the minimum pressure point. Subsequent studies have demonstrated that inception involves intermittent and short-lived attachment of travelling bubble cavitation to the surface near the minimum pressure point (Blake, Wolpert & Geib 1977; Ceccio & Brennen 1991; De Chizelle, Ceccio & Brennen 1995; Li & Ceccio 1996; Laberteaux *et al.* 1998; George, Iyer & Ceccio 2000). The important role of boundary layers was discussed first by Arakeri & Acosta (1973). They and subsequently Gates & Acosta (1979) and Katz (1984) showed that laminar boundary layer separation occurs on the hemispherical headforms, and, under such conditions, the onset of cavitation involves entrainment of free-stream nuclei into the relatively quiescent separated region, followed by cavity growth.

These observations raise questions on how stable attached cavitation occurs for cases without laminar separation. However, until recently, technical limitations have prevented quantitative assessment of the interaction between bubbles and the flow in the inner part of boundary layers. It is also unclear why some forms of cavitation, such as travelling bubble cavitation and the associated transient attachment to the surface, are very sensitive to the concentration of free-stream (or surface) nuclei, whereas the onset of sheet cavitation is relatively insensitive (Gates & Acosta 1979), and sustains itself once it starts.

In their experiments, Parkin & Kermeen (1953) noticed isolated stationary microbubbles growing on the surface in the vicinity of the attached cavity and then get swept by the free-stream flow after a few milliseconds. They assumed that these bubbles grow by diffusion of non-condensable gas. To model this process, Van Wijngaarden (1967) calculated the time required for a spherical bubble to grow by advective gas diffusion, assuming that this bubble is subjected to the free-stream flow. Most of the subsequent studies have concluded or assumed that gas diffusion is not a significant contributor to the cavitation inception owing to the long time scales involved (Plesset & Prosperetti 1977; Brennen 2013).

The present combination of high-speed imaging and velocity measurements that resolve the boundary layer in the vicinity of the minimum pressure point on a curved surface addresses the questions raised above. We show that the mechanism sustaining attached cavitation involves upstream migration of numerous microbubbles originating from a previous collapse of attached cavities. In the case where the boundary layer separates, these bubbles are trapped in the low-momentum recirculating flow. In a non-separated flow, the bubbles are driven upstream by the large adverse gradients downstream of the minimum pressure point after being trapped in the low-speed region where the boundary layer is thickened. Hence, in both cases the process becomes insensitive to free-stream nuclei. In cases where the boundary layer remains thin, there is no upstream migration, and the attached cavitation is intermittent and initiated primarily by travelling bubble cavitation. Furthermore, as the microbubbles migrate upstream for a few milliseconds, they grow significantly by gas diffusion in the supersaturated low-pressure region. When they reach a size comparable to that of the low-momentum zone, either they are swept by the external flow or they initiate a new cavitation event. Hence, gas diffusion plays an important role
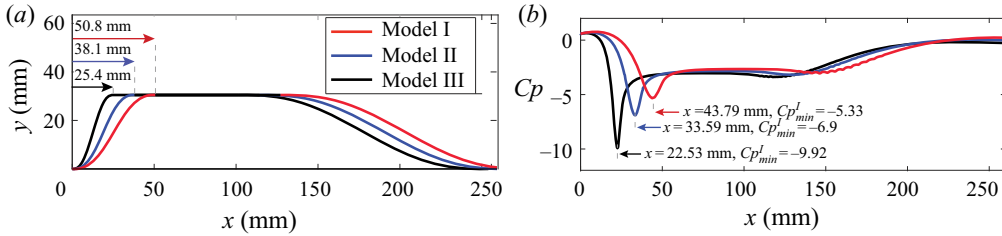
901 R4-2

FIGURE 1. (*a*) The contoured nozzles' geometry, and (*b*) computed pressure coefficient along their surface.

in the process sustaining attached cavitation. The experimental set-up and procedures are summarized in the next section. Results are presented in § 3, followed by conclusions in § 4.

2. Experimental set-up

The experiments have been performed in a small high-speed water tunnel, as described in Gopalan & Katz (2000). The flow is driven by two 15 HP centrifugal pumps located 5 m below the test section to minimize the pump cavitation, and passes through a 1000 litre buffer tank, where free-stream bubbles are removed. The test section dimensions are $63.5\,\text{mm} \times 50.8\,\text{mm} \times 350\,\text{mm}$ and have windows on all sides. This facility is equipped with pressure transducers and means to control the mean pressure. The bottom window of the test section has been replaced by three different transparent contoured nozzles, all with a maximum height of 30 mm, thus reducing the cross-section by 50 %. The geometry of these nozzles, which are shown in figure 1(*a*), has been designed to mimic the suction side of lifting surfaces, which typically have distinct local pressure minima. The shape of their forward-facing side is defined using fifth-order polynomials with beginning and ending tangent to the horizontal direction, where the curvature also diminishes. The variations in minimum pressure are generated by varying the length of the curved fronts. The corresponding distributions of pressure coefficient along the bottom wall, $Cp = (P - P_{in})/0.5\rho V_{in}^2$, where P_{in} and V_{in} are the pressure and velocity at the inlet to the test section, respectively, and P is the local pressure, are presented in figure 1(*b*). They have been determined using inviscid simulations of the flow in the resulting two-dimensional (2-D) nozzles using Ansys Fluent.

These simplified simulations have only been used as guidance during the design phase. Model I has the mildest negative pressure peak and adverse pressure gradients around it, and model III has the steepest gradients and lowest pressure peak. As shown by the experimental data, the boundary layers for models I and II remain attached, but the latter already has an inflection point with a thin low-momentum zone under it. In contrast, the boundary layer separates for model III, giving us three distinctly different flow conditions. These models have been machined and polished to establish a smooth surface, allowing the boundary layer to remain laminar, at least until the minimum pressure point, and, as the observations indicate, surface nuclei are not a significant contributor to the onset of cavitation. In all cases, the test conditions focus on the behaviour of cavitation slightly below the inception level of patchy attached cavitation. Consequently, the local pressures or cavitation indices, namely the local values of $\sigma + Cp$, are similar. Specific information is provided in the next section.

The velocity distribution around the minimum pressure point has been measured using high-resolution 2-D particle image velocimetry (PIV), where the boundary layer
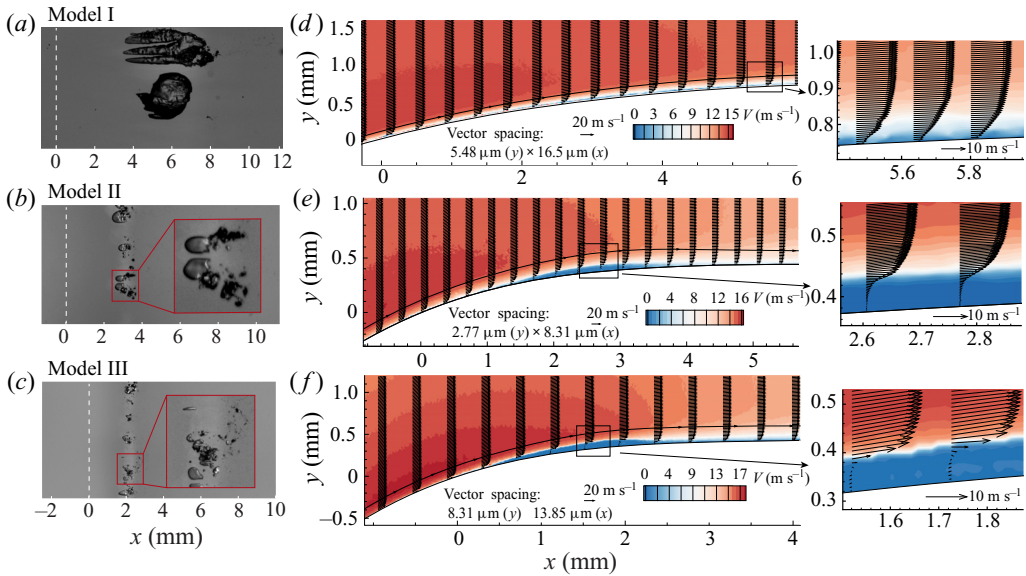
FIGURE 2. (*a–c*) Snapshots of incipient attached cavitation for models I, II and III, respectively, with insets showing 3× magnified sections. (*d–f*) Corresponding contours of measured mean velocity magnitude.

thickness is of the order of 100 μm. The images are recorded using a charge-coupled device (CCD) camera with a resolution of 6600×4400 pixels (Imperx 29 MP) fitted with a Nikon-Micro 105 mm lens and a Nikon 2× teleconverter to achieve a spatial resolution of 2.77 μm pixel^{-1}. The laser sheet illuminating the central plane of the test section is generated by a Quantel EverGreen 200 laser. The flow is seeded with 2 μm silver-coated glass spheres. All the velocity measurements are performed at pressures that are substantially higher than the cavitation inception level. The mean velocity is determined using the sum of correlation technique (Meinhart, Wereley & Santiago 2000), which determines the displacement from an ensemble-averaged cross-correlation over small interrogation windows with sizes varying between 3×1 and 6×3 pixels in the horizontal and vertical directions, respectively. As many as 20 000 image pairs are required to obtain converged results for such small areas. There is no overlap between windows. The interrogation windows are specified next to their respective velocity map in figure 2. Silhouette imaging, where the camera faces a 100 W diffused mercury arc lamp, is used for recording the cavitation events. A high-speed camera (Phantom V2640) fitted with a 105 mm lens, a 100 mm extension ring and a 2× teleconverter is used for acquiring 1024×512 pixel images at 44 000 frames per second and a resolution of 5.48 μm pixel^{-1}. Lower-magnification (34 μm pixel^{-1}) data at the same frame rate and image size are also recorded to obtain broader views.

3. Results

3.1. *The mechanism that sustains the attached cavitation*

Figure 2 presents characteristic snapshots of early phases of attached cavitation for models I, II and III, when the pressure in the facility is reduced slightly below the level

901 R4-4

Model	P_{in} (bar)	V_{in} (m s^{-1})	$V_{s,max}$ (m s^{-1})	Cp_{min}^B	Cp_{min}^I	σ	$Cp_{min}^B + \sigma$
I	0.850	5.86	14.68	-5.43	-5.33	4.82	-0.61
II	1.035	5.86	16.03	-6.48	-6.90	5.88	-0.59
III	1.375	5.86	18.27	-8.72	-9.92	7.87	-0.85

TABLE 1. The present experimental conditions.

where attached cavitation inception occurs. The corresponding movies showing magnified views of the cavitation are provided as supplementary movies 1–3 available at https://doi.org/10.1017/jfm.2020.646. The respective measured mean velocity maps are presented to the right of each image, with insets highlighting the regions where attached cavitation inception occurs downstream of the minimum pressure point. In each plot, the origin of the coordinate system is located at the estimated point of minimum radius of surface curvature based on the intersection of the light sheet with the surface. Related variables are listed in table 1, including: (i) P_{in} and V_{in}, the pressure and velocity, respectively, at the entrance to the test section, which are used as the reference values in the definition of Cp; (ii) $V_{s,max}$, the maximum velocity along a streamline, V_s, located just outside of the boundary layer; (iii) Cp_{min}^B, the minimum pressure coefficient calculated using Bernoulli's equation; (iv) Cp_{min}^I, the estimated pressure coefficient from the inviscid simulations (figure 1b); (v) σ, the cavitation index during the cavitation tests; and (vi) $Cp_{min}^B + \sigma$, the cavitation index based on the local pressure. The differences between Cp_{min}^B and Cp_{min}^I increase from 1.9 % to 6 % and to 11.5 % as the surface radius of curvature decreases, an expected trend owing to the increase in boundary layer thickness. Note also that the cavitation indices near the minimum pressure point, namely $Cp_{min}^B + \sigma$, during the imaging tests are negative, as expected. For reasons elucidated in the following sections, the early stages of attached cavitation occur downstream of the minimum pressure point, where the values of the local $Cp^B + \sigma$ fall in the range 0.1–0.2, and corresponding absolute pressures vary between 3.5 and 6 kPa.

For model I, the cavitation patches are approximately 5 mm long, isolated and form only as travelling bubble cavitation events attach to the surface downstream of the minimum pressure point, consistent with the observations of Ceccio & Brennen (1991) and De Chizelle *et al.* (1995). These patches remain attached for 2–10 ms before collapsing, becoming fragmented and being swept away. Conversely, the cavitation formed in the other two models is characterized by smaller (1–2 mm) patches that are distributed along the span of the nozzle, with those corresponding to model II being slightly longer than those seen for model III. While each patch still persists for a few milliseconds, new ones form repeatedly, such that the attached cavitation rarely disappears from the field of view once it starts. While the initial patch appears to be generated by occasional travelling bubble cavitation, the subsequent ones do not, raising questions about their origin and the mechanisms sustaining them. The answers can be found by examining the local boundary layer structure and by observations on the processes that initiate the subsequent patches.

A few observations can be made from the mean velocity fields presented in figure 2 and the magnified insets attached to each plot, which focus on the regions of attached cavitation. Having the mildest adverse pressure gradient, the boundary layer for model I remains thin downstream of the minimum pressure point (figure 2d), and the velocity magnitude exceeds 2.8 m s^{-1} as close as 10 µm from the surface. Estimating the thickness

of the boundary layer in the inset area based on the average height where the velocity reaches 95 % of the maximum value gives $\delta_{95} = 90$ μm. In contrast, the adverse pressure gradient for model II (figure 2*e*) is strong enough to cause local thickening of the boundary layers ($\delta_{95} = 160$ μm) and the formation of a 60–80 μm thick, 3.5–4 mm long, low-momentum zone under an inflection point. Yet, the mean velocity there remains positive with magnitude that does not exceed 0.3–0.4 m s^{-1}, i.e. there is no mean flow separation. Furthermore, examination of approximately 200 samples of particle displacement do not show instantaneous reverse flows. The boundary layer for model III (figure 2*f*) does separate, causing formation of an approximately 80 μm thick recirculating zone with peak reverse velocity of 0.6–0.7 m s^{-1}. Here, $\delta_{95} = 200$ μm while the separation and reattachment points, estimated based on the location of zero wall-normal velocity gradients close to the surface, are $x = 0.6$ and 2.25 mm, respectively. These observations suggest that there is a causal relationship between the occurrence of sustained attached cavitation patches for models II and III and the formation of low-momentum zones near the surface. The following observations elucidate the mechanisms involved.

Figure 3(*a*) is a sample image of attached cavitation for model II, taken from supplementary movie 2. It shows several attached cavitation patches along with more than 20 microbubbles with sizes ranging between 20 and 50 μm moving upstream towards the minimum pressure line. The bubble tracks over a period of 2.2 ms prior to acquiring this image along with the instantaneous direction of these bubbles are superimposed. The tracking has been performed using the 'ImageJ Trackmate' software (Tinevez *et al.* 2017), and verified manually. Supplementary movie 2 shows that the cavitation patches appear intermittently and disappear in a few milliseconds at the downstream end of the low-momentum zone. As they evolve, these patches grow, propagate laterally and split frequently. They disappear either by being fragmented, with the sub-patches getting swept into the free stream, or by collapsing, starting from their downstream end. This collapse appears as an upstream-propagating vapour–liquid front until the patch disappears. Both processes leave a large number of residual microbubbles. Most of them get swept immediately downstream, as seen in multiple prior studies (e.g. Russell *et al.* 2016). However, as illustrated by the tracks, a small fraction of these microbubbles migrate upstream and laterally, in what appears to be erratic trajectories, within the low-momentum zone of the boundary layer. The typical size of these bubbles is smaller than or comparable to the height of this zone.

The duration of their generally upstream migration varies from 2 to 16 ms at mean velocities that range between 0.5 and 0.7 m s^{-1} until they either get swept by the free-stream flow or become a nucleation site of a new cavitation patch. The location of the new patch does not appear to be correlated with that of previous events, and often occurs away from other sites with attached cavitation. As a demonstration of a case leading to cavitation inception, figures 3(*b*) and 3(*c*) follow the time history of a single bubble, with the first series showing the full trajectory at relatively coarse time steps, and the second focusing on the last 431 μs, when the new attached patch forms. This microbubble migrates upstream for approximately 2.35 ms at a mean velocity of 0.62 m s^{-1}, i.e. 3.9 % of the maximum velocity, and then grows rapidly, as its size increases from 30 μm to approximately 300 μm in less than 200 μs. Hence, the bubble dynamics involves two time scales, with the upstream migration occurring in milliseconds, and the cavitation inception in tens of microseconds. Once the initial attachment of travelling bubble cavitation occurs and generates the first group of microbubbles trapped in the inner part of the (non-separated) boundary layer, the upstream migration, formation of new cavitation patches, followed by their collapse, generation of new microbubbles and
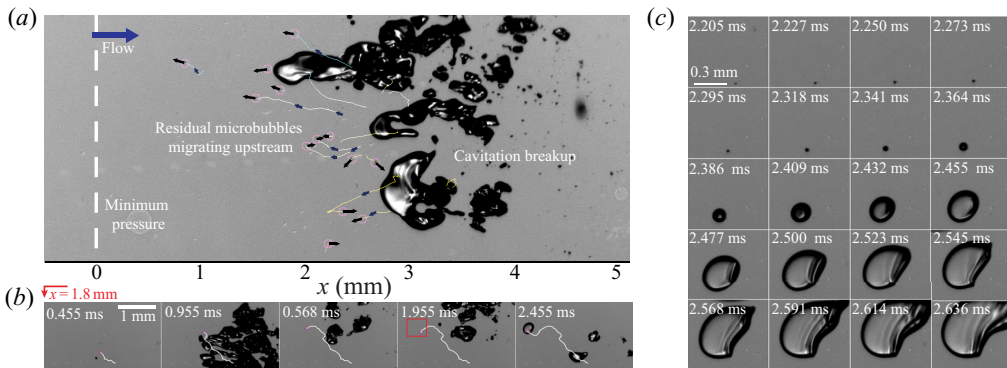
FIGURE 3. (*a*) Tracks of microbubbles migrating upstream in the low-momentum region of model II superimposed on a cavitation snapshot. (*b*) A 2.5 ms time series focusing on a bubble track leading attached cavitation inception. (*c*) The red area marked in (*b*) enlarged to show the rapid growth in the final 431 µs.

so on, sustains the intermittent formation of attached cavitation. As discussed below, the upstream migration of the bubbles against the local slow flow is induced by the adverse pressure gradients in this part of the flow field.

The mechanism sustaining cavitation for model III (supplementary movie 3) appears to be similar to those described above, with some differences that can be largely attributed to the separated flow in the inception area. The attached patches grow to smaller lengths and remain confined to the separated region. They also fragment at a faster rate and are more evenly dispersed along the tangential direction. Moreover, the number of microbubbles seen migrating upstream appears to be about twice as large compared to the non-separated flow, resulting in more frequent inception events of attached cavitation. As elaborated in the next section, which discusses the bubble dynamics, in this case the microbubbles are driven upstream with the reverse flow in the recirculation region.

3.2. *Microbubble dynamics*

Figure 4(*a–f*) depicts the results of statistical analysis performed based on 915 bubble tracks for model II (figure 4*a,c,e*) and 700 tracks for model III (figure 4*b,d,f*), each providing multiple data points. Joint probability distributions of normalized bubble velocity components and streamwise location are presented in figures 4(*a,b*) and 4(*c,d*) for the streamwise ($V_{bx}/V_{s,max}$) and lateral ($V_{bz}/V_{s,max}$) components, respectively. The corresponding locations of the thickened boundary layers are also provided. Matching probability density functions (p.d.f.s) of the normalized velocity magnitude, $\tilde{V} = V_b/V_{s,max}$, are presented in figure 4(*e,f*). Several trends appear to be similar. First, the lateral velocity components are symmetric, indicating that the lateral motions do not have a preferred direction. Second, the streamwise velocity components decrease as the bubbles migrate upstream towards the minimum pressure point ($x = 0$), away from their origin where the cavitation collapses. Third, in both cases, the microbubbles are concentrated inside the low-momentum region, hence they are spread over a longer area for model II. Finally, as illustrated by the blue lines (figure 4*e,f*), both p.d.f.s of velocity magnitude appear to have a Rayleigh distribution, i.e. $P(\tilde{V}) = (2\tilde{V}/\langle \tilde{V}^2 \rangle) \exp(-\tilde{V}^2/\langle \tilde{V}^2 \rangle)$. Such behaviour has been attributed to random horizontal motions of a particle suspended
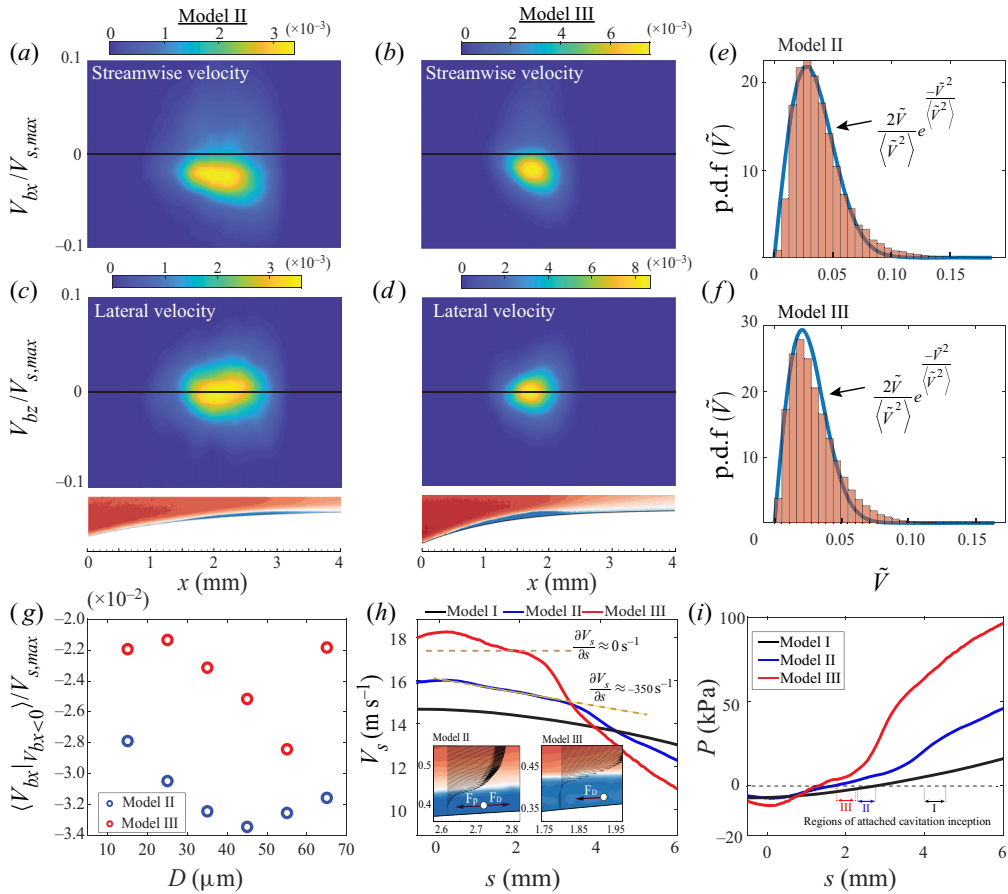
901 R4-7

FIGURE 4. (*a–d*) P.d.f.s of streamwise (*a,b*) and lateral (*c,d*) bubble velocities for (*a,c*) model II and (*b,d*) model III. (*e,f*) P.d.f.s of bubble velocity magnitude for (*e*) model II and (*f*) model III. (*g*) The mean bubble velocity during upstream migration plotted versus the diameter. (*h*) Velocity distribution and (*i*) corresponding pressure along streamlines located just outside of the boundary layer calculated using Bernoulli's equation.

close to dynamic equilibrium in a fluctuating flow of a fluidized bed, i.e. when the mean force balance on it is zero (Ojha *et al.* 2004). Hence, the p.d.f.s in figure 4(*e,f*) suggest that the present microbubbles are nearly in dynamic equilibrium with their surrounding flow field.

The measured mean bubble velocities conditioned on upstream motion (that is, $\langle V_{bx}|_{V_{bx}<0}\rangle/V_{s,max}$) are plotted as a function of their diameter in figure 4(*g*). While they migrate upstream in both cases, the mechanisms driving them are different, as illustrated by the inset in figure 4(*h*). For model III, the microbubbles are driven in the same direction as the flow in the recirculating region of the separated boundary layer. In this case, the pressure gradients are nearly zero, as indicated by the streamwise velocity and pressure profiles along a streamline located just outside of the boundary layer shown in figure 4(*h,i*). The pressure is calculated from the measured velocity using Bernoulli's equation. Hence, the primary likely force driving the bubbles upstream is drag. As expected, the measured values, ranging from -0.028 to -0.022, are smaller, but of the same order as the normalized maximum liquid reverse flow within the separated region, -0.033 to -0.028.

This relationship supports our postulate that the motion of these bubbles is dominated by the drag force. For $D > 55\ \mu\text{m}$, when the bubble diameter becomes comparable to the separated region height, the upstream velocity decreases sharply, presumably owing to the growing influence of the positive velocity in the outer part of the separated region.

In contrast, near model II, the microbubbles located in the inner part of the boundary layer move against the local flow, where they are subjected to adverse pressure gradients evident from the velocity and pressure distributions (figure 4*h,i*). Being in near-hydrodynamic equilibrium, as the p.d.f.s suggest, the force induced by the pressure gradients is likely to be balanced by the drag force (neglecting inertia and lift, etc.). Equating these forces (inset in figure 4*h*) leads to the following estimate for the local relative velocity: $V_{b,rel} = \sqrt{(4D/3C_D)(-V_s\partial V_s/\partial s)}$. Here, $C_D = (24/Re)(1 + 0.15Re^{0.681}) + 0.407Re/(Re + 8710)$ is the drag coefficient estimated according to Brown & Lawler (2003), D is the bubble diameter, and Re is the bubble Reynolds number estimated based on mean slip velocity. Using the measured value, $V_s\partial V_s/\partial s \approx -5.3 \times 10^3\ \text{m s}^{-2}$, gives $V_{b,rel}/V_{s,max} \approx -0.006$ and -0.03 for $D = 20$ and 60 μm, respectively. For $D < 50\ \mu\text{m}$, $\langle V_{bx}|_{V_{bx}<0}\rangle/V_{s,max}$ increases with diameter (figure 4*g*), but at a slower rate than $V_{b,rel}$, with the estimated and measured values agreeing at $D \approx 35\ \mu\text{m}$. Note that, owing to very low local flow velocity, V_b is very close to $V_{b,rel}$. The disagreement in trends might be associated in part with the simplified model, the impact of the collapsing cavities, as well as the uncertainty in measuring the microbubble diameter, estimated as 5 μm based on the pixel resolution. For $D > 45\ \mu\text{m}$, the upstream mean velocity decreases presumably since the diameter becomes comparable to the low-momentum thickness, i.e. part of the bubble is influenced by faster downstream flows.

It should be emphasized that the present analysis is based on the mean flow field, without cavitation. The growth and collapse of cavities inherently generate local unsteady flows that are likely to affect the bubble trajectories. In fact, the above-mentioned random motions (figure 4*e,f*), as well as the broad distributions of velocities, including lateral ones (see figure 4*a–d* and supplementary movies 2 and 3), are likely to be affected by the intermittent growth and collapse of the cavities. However, on average the bubbles migrate upstream at a low mean velocity, whether they are located near to or away from the collapsing cavities (figure 4*g*). Hence, the simplified models balancing the effects of pressure gradients and drag for model II, and drag only for model III, seem to be reasonable. The results show that, owing to the very high local acceleration (5000 m s^{-2}) in the region of bubble migration for model II, the microbubbles cannot be treated as passive scalars.

The next discussion examines the impact of non-condensable gas diffusion on the size of the bubbles migrating upstream. Our observations indicate that,over the few milliseconds of migration, these bubbles grow from a typical initial diameter of 10–20 μm to 40–50 μm. The latter is already comparable to that of the thickness of the low-momentum region of the boundary layer. At this stage they either grow explosively or are swept downstream. Figure 5(*a*) demonstrate this growth, where a microbubble grows from a diameter of 11 μm to 38.3 μm in 6 ms, before being swept downstream by the free-stream flow. The measured size for 12 other microbubbles as a function of time is presented in figure 5(*b*). Initially they all grow at a relatively mild rate for 2–10 ms, and then either grow explosively in tens of microseconds, namely cavitate, or get swept. The relatively slow growth rate that occurs during the above-mentioned long time scale could be caused either by non-condensable gas diffusion or by the change in the local pressure. The latter can be discounted since the bubbles migrate upstream by an average distance of 0.4 mm with peak values of
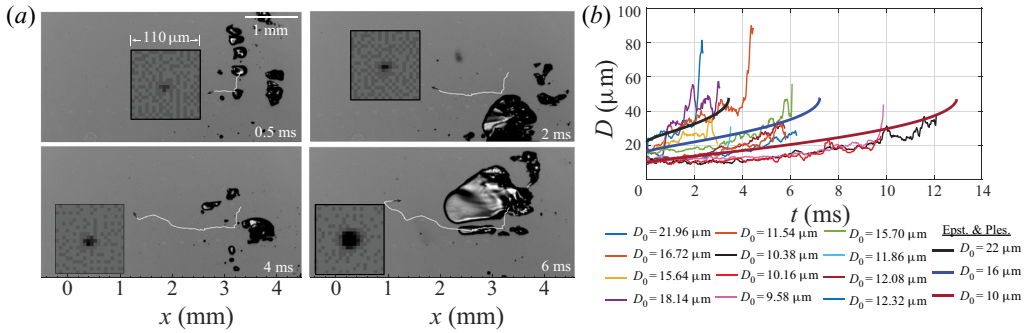
FIGURE 5. (*a*) A time series showing the growth of a microbubble during its 6 ms migration upstream, and (*b*) measured size evolution of 12 sample microbubbles superimposed on the calculated growth by mass diffusion.

approximately 2 mm. The corresponding changes to the local pressure are 2.1 and 10.6 kPa, respectively. After subtracting the vapour pressure, and accounting for $4\tau/D$, where τ is the surface tension, the partial pressure of non-condensable gas in a 10 µm diameter bubble changes at most from 34.4 to 24 kPa (2 mm displacement). Assuming isothermal expansion, the bubble radius would increase by 13 %. In contrast, figure 5(*a*) and several other examples in figure 5(*b*) shows that the typical diameter increases by 3–4 times. Hence, gas diffusion must be playing a prominent role.

Owing to the very low liquid pressure in the cavitation inception area, the fluid becomes locally supersaturated with non-condensable gases. Following Epstein & Plesset (1950), the growth rate of a stationary bubble by mass diffusion is $dD/dt = \alpha[(D/2)^{-1} + (\pi\kappa t)^{-0.5}]$, where $\alpha = 2\kappa\mathcal{R}T(C_\infty - C_s)/(P - P_v + 8\tau/3D)$, κ is the diffusion coefficient of air in water, $\mathcal{R}$ is the gas constant of air, C_∞ is the dissolved gas concentration far from the bubble ($C_\infty = 18.2$ mg$_{air}$ l^{-1} in the present experiments) and C_s is the pressure-dependent saturation concentration. Note that, under the present conditions, the magnitude of the surface tension term, e.g. 20 kPa for a 10 µm bubble and 5 kPa for a 40 µm bubble, is the largest contributor to the pressure inside the bubble. As the bubble grows, the contribution of this term diminishes. According to Fuller, Schettler & Giddings (1966), the diffusion coefficient increases with decreasing pressure according to $\kappa/\kappa_0 = (P_0/P)(T/T_0)^{1.75}$, where $\kappa_0 = 2 \times 10^{-5}$ cm^2 s^{-1} for $P_0 = 101$ kPa and $T_0 = 293.2$ K. While the above relation has been validated only down to an ambient pressure of 35 kPa (Li *et al.* 2014), in the present assessment we extrapolate it to the pressure at the origin of the bubble, 8 kPa. The result, $\kappa \approx 2.5 \times 10^{-4}$ cm^2 s^{-1}, is an order of magnitude higher than that of atmospheric values. Figure 5(*b*) compares the measured time evolution of bubble diameter for 12 sample microbubbles to that obtained by integrating the Epstein & Plesset (1950) solution using the aforementioned κ, C_∞ and $C_s = 1.44$ mg$_{air}$ l^{-1} at 8 kPa, and the same initial diameter. The trends appear to be quite similar until some of the bubbles begin to grow explosively, once cavitation inception starts. While the model simplifies the processes involved, this comparison and lack of other plausible explanations strongly suggest that bubble growth is caused primarily by non-condensable gas diffusion.

The present observations also provide a plausible explanation for why the attached cavitation inception occurs systematically downstream of the minimum pressure point, and why it does not occur shortly after being generated in the regions where the previous cavities collapse. Starting from the latter, the microbubbles form at the downstream end

of the collapsing cavities for models II and III, where the absolute mean liquid pressure varies between 5 and 20 kPa. Owing to the surface tension, the resulting pressure inside a (for example) 10 µm diameter bubble is 35–50 kPa. In this area, it would be very difficult to satisfy the condition for unstable bubble growth, namely $P - P_v < -8\tau/3D$. As these bubbles migrate upstream while growing by mass diffusion, their interior pressure decreases owing to both reductions in the absolute local pressure and the magnitude of $4\tau/D$, with the latter changing at a faster rate. Yet, the mean liquid pressure in the area where cavitation inception typically occurs remains positive (but very low – see figure 4*i*). Hence, the condition for unstable bubble growth cannot be satisfied by the mean flow alone. However, it could occur intermittently, owing to local pressure fluctuations induced by the flow or by collapse of a previous attached cavitation event further downstream. With the increase in bubble diameter, the amplitude of fluctuations required for triggering the instability decreases. For sufficient growth by mass diffusion to occur, the bubble has to be located within the low-momentum zone of the boundary layer. Even there, only some of the bubbles initiate attached cavitation while others are swept rapidly downstream by the external flow. These observations imply that the bubbles cannot migrate upstream all the way to the minimum pressure point, where the inner part of the boundary layer is very thin, and the pressure gradient diminishes.

4. Conclusions

In cases where adverse pressure gradients either thicken the boundary layer or cause local flow separation, the inner region of low momentum 'shelters' microbubbles from being swept by the main flow. The origin of these trapped microbubbles can be traced back to intermittent attachment and collapse of travelling bubble cavitation events originating from free-stream nuclei. Without flow separation (model II), there is no other mechanism that could drive free-stream microbubbles into the thin low-momentum zone. Being largely laminar, there is very little wall-normal mixing, and adverse pressure gradients are not sufficient to drive the bubble upstream in high-momentum regions above or downstream of the thickened boundary layer. Furthermore, by tracking them to their origin, and the fact that we have not observed patches originating from unidentified sources, surface nuclei do not seem to play a significant role in the present study. When the flow is separated, while prior studies have suggested that free-stream nuclei might be entrained through the reattachment area (Arakeri & Acosta 1973), they do not seem to play a major role in the present study.

In the non-separated boundary layer, the trapped bubbles are driven upstream by the adverse pressure gradients, and, when the flow is separated, the pressure gradients diminish, and the bubbles are driven upstream by drag. Both cases result in slow upstream migration that lasts a few milliseconds. During that time the microbubbles grow by 3–4 times owing to non-condensable gas diffusion until their size becomes comparable to the thickness of the low-momentum region. At this stage, some are swept downstream, but others become nucleation sites for new attached cavitation events. When the new patches collapse, they generate new residual microbubbles, allowing the process to repeat itself independently of free-stream nuclei. In both cases, thickening of the boundary layer is a common key feature that sustains the continuous bubble migration and growth leading to regeneration of attached cavitation. The bubble migration and self-sustaining mechanisms occurring over models II and III do not occur over model I even when the pressure is reduced further. In this case, the adverse pressure gradients are too mild to thicken the boundary layer and create a region where the bubbles can be sheltered. With

decreasing adverse pressure gradients, the force driving the bubbles upstream against the mean flow also diminishes. These observations provide a plausible answer to the following longstanding question: Why, and under what conditions, is inception of attached cavitation on curved surfaces or hydrofoils at incidence relatively insensitive to the concentration of free-stream nuclei?

Acknowledgements

Declaration of interests

The authors report no conflict of interest.

Supplementary movies

Supplementary movies are available at https://doi.org/10.1017/jfm.2020.646.

References

ARAKERI, V. H. & ACOSTA, A. J. 1973 Viscous effects in the inception of cavitation on axisymmetric bodies. *Trans. ASME J. Fluids Engng* **95** (4), 519–527.

ARNDT, R. E. A. 2002 Cavitation in vortical flows. *Annu. Rev. Fluid Mech.* **34** (1), 143–175.

BLAKE, W. K., WOLPERT, M. J. & GEIB, F. E. 1977 Cavitation noise and inception as influenced by boundary-layer development on a hydrofoil. *J. Fluid Mech.* **80** (4), 617–640.

BRENNEN, C. E. 2013 *Cavitation and Bubble Dynamics*. Cambridge University Press.

BROWN, P. P. & LAWLER, D. F. 2003 Sphere drag and settling velocity revisited. *J. Environ. Engng* **129** (3), 222–231.

CECCIO, S. L. & BRENNEN, C. E. 1991 Observations of the dynamics and acoustics of travelling bubble cavitation. *J. Fluid Mech.* **233**, 633–660.

DE CHIZELLE, Y. K., CECCIO, S. L. & BRENNEN, C. E. 1995 Observations and scaling of travelling bubble cavitation. *J. Fluid Mech.* **293**, 99–126.

EPSTEIN, P. S. & PLESSET, M. S. 1950 On the stability of gas bubbles in liquid–gas solutions. *J. Chem. Phys.* **18** (11), 1505–1509.

FULLER, E. N., SCHETTLER, P. D. & GIDDINGS, J. C. 1966 New method for prediction of binary gas-phase diffusion coefficients. *Ind. Engng Chem.* **58** (5), 18–27.

GATES, E. M. & ACOSTA, A. J. 1979 Some effects of several free stream factors on cavitation inception on axisymmetric bodies. In *Proceedings 12th Symposium on Naval Hydrodynamics, Washington, DC*, pp. 86–108. National Academy of Sciences.

GEORGE, D. L., IYER, C. O. & CECCIO, S. L. 2000 Measurement of the bubbly flow beneath partial attached cavities using electrical impedance probes. *Trans. ASME J. Fluids Engng* **122** (1), 151–155.

GOPALAN, S. & KATZ, J. 2000 Flow structure and modeling issues in the closure region of attached cavitation. *Phys. Fluids* **12** (4), 895–911.

KATZ, J. 1984 Cavitation phenomena within regions of flow separation. *J. Fluid Mech.* **140**, 397–436.

LABERTEAUX, K. R., CECCIO, S. L., MASTROCOLA, V. J. & LOWRANCE, J. L. 1998 High speed digital imaging of cavitating vortices. *Exp. Fluids* **24** (5–6), 489–498.

LI, C. Y. & CECCIO, S. L. 1996 Interaction of single travelling bubbles with the boundary layer and attached cavitation. *J. Fluid Mech.* **322**, 329–353.

LI, J., CHEN, H., ZHOU, W., WU, B., STOYANOV, S. D. & PELAN, E. G. 2014 Growth of bubbles on a solid surface in response to a pressure reduction. *Langmuir* **30** (15), 4223–4228.

MEINHART, C. D., WERELEY, S. T. & SANTIAGO, J. G. 2000 A PIV algorithm for estimating time-averaged velocity fields. *Trans. ASME J. Fluids Engng* **122** (2), 285–289.

OJHA, R. P., LEMIEUX, P. A., DIXON, P. K., LIU, A. J. & DURIAN, D. J. 2004 Statistical mechanics of a gas-fluidized particle. *Nature* **427** (6974), 521–523.

PARKIN, B. R. & KERMEEN, R. W. 1953 Incipient cavitation and boundary layer interaction on a streamlined body. *Tech Rep.* California Institute of Technology.

PLESSET, M. S. & PROSPERETTI, A. 1977 Bubble dynamics and cavitation. *Annu. Rev. Fluid Mech.* **9** (1), 145–185.

RUSSELL, P. S., GIOSIO, D. R., VENNING, J. A., PEARCE, B. W., BRANDNER, P. A. & CECCIO, S. 2016 Microbubble generation from condensation and turbulent breakup of sheet cavitation. In *31st Symposium on Naval Hydrodynamics*, pp. 11–16. Office of Naval Research, USA.

TINEVEZ, J., PERRY, N., SCHINDELIN, J., HOOPES, G. M., REYNOLDS, G. D., LAPLANTINE, E., BEDNAREK, S. Y., SHORTE, S. L. & ELICEIRI, K. W. 2017 Trackmate: an open and extensible platform for single-particle tracking. *Methods* **115**, 80–90.

VAN WIJNGAARDEN, L. 1967 On the growth of small cavitation bubbles by convective diffusion. *Intl J. Heat Mass Transfer* **10** (2), 127–134.